Specifically designed 10-Fe$_1$Mn$_1$-USY hydrophobicity material for acetone adsorption under high humidity condition

Nhat-Thien Nguyen[1], Thi-Minh-Phuong Nguyen[2,3,4], Alvin-R Caparanga[3,4], Yi-Ren Chiu[5], Cong-Chinh Duong[6], Thi-Thanh Duong[7], Chung-Yu Guan[5], Gui-Bing Hong[1] and Chang-Tang Chang[5*]

Abstract

Acetone is a solvent used in many laboratories and factories. Serious problems will occur when it is exposed to the environment. Therefore, a new design hydrophobicity bimetallic metal material (10-Fe$_1$Mn$_1$-USY) was prepared for acetone adsorption under conditions of high humidity. Hydrophobic Y type zeolite was used to prepare bimetallic metal materials and the effect of different operating parameters (including different material, humidity, temperature, pollutant concentration, residence time, and regeneration) on the efficiency of acetone treatment was examined. Isothermal adsorption model, kinetics and thermodynamic model analysis were also used to establish the reaction mechanism. The 10-Fe$_1$Mn$_1$-USY material has good adsorption capacity (133 mg g^{-1}) for acetone under a relative humidity of 50%. The main factors affecting the adsorption capacity are the contact angle, hydrophobicity, specific surface area, and Si/Al of the material. The isothermal adsorption and the kinetic adsorption behavior of 10-Fe$_1$Mn$_1$-USY material for acetone are more suitable for the Temkin isotherm adsorption model and the pseudo-first-order kinetic model. The adsorption of acetone by 10-Fe$_1$Mn$_1$-USY material is dominated by intra-particle diffusion. According to the thermodynamic analysis results, the adsorption behavior of 10-Fe$_1$Mn$_1$-USY material for acetone is a type of physical adsorption, and a spontaneous and non-sequential reaction.

Keywords FeMn-USY, Acetone, High humidity, Low temperature, Hydrophobic material

*Correspondence:
Chang-Tang Chang
ctchang@niu.edu.tw
[1] Department of Chemical Engineering and Biotechnology, National Taipei University of Technology, Taipei 10608, Taiwan
[2] Faculty of Environmental and Natural Sciences, Duy Tan University, Da Nang 550000, Vietnam
[3] Institute of Research and Development, Duy Tan University, Da Nang 550000, Vietnam
[4] School of Chemical Engineering and Chemistry, Mapua Institute of Technology, 1002 Manila, Philippines
[5] Department of Environmental Engineering, National Ilan University, Yilan City 26047, Taiwan
[6] Southern Institute of Water Resources Research, Ho Chi Minh City 700000, Vietnam
[7] Faculty of Environment and Natural Resources, Ho Chi Minh City University of Technology, Ho Chi Minh City 700000, Vietnam

1 Introduction

As one of the representative ketones of Volatile Organic Compounds (VOCs), acetone is an important chemical raw material and solvent [1, 2]. It is extremely harmful to the environment and the human body, making the prevention and control of acetone pollution critical [3, 4]. At present, common treatment methods of VOCs include the condensation [5], absorption [6], plasma destruction [7], thermal incineration [8], catalyst incineration [9], photocatalytic [10, 11] and adsorption [12, 13] methods. The condensing method has limited treatment efficiency and cannot treat exhaust gas containing various pollutant components. Absorption methods are prone to waste-water treatment problems and high maintenance costs. The plasma destruction method is prone to interference,

Nguyen *et al. Sustainable Environment Research*   (2023) 33:15

Page 2 of 15

requires expensive equipment and has high maintenance costs. The thermal incineration and catalyst incineration methods require higher temperatures to destroy pollutants, wasting energy, and creating secondary pollutant problems that increase the cost of secondary treatment. Therefore, the adsorption method is the most promising technology in the treatment of VOCs. The adsorption method can simultaneously treat multiple components of pollutants, but is easily affected by the humidity of the exhaust gas, which absorbs water vapor easily, resulting in material adsorption saturation. Hence, a new design for a hydrophobicity bimetallic metal material was prepared for adsorption VOCs under high humidity conditions in this study.

Several studies on the adsorptive removal of various VOCs have been reported. Zhang et al. [14] conducted a comparative study on the adsorption of toluene over MCM-41 (Mobil Composition of Matter No. 41) and SBA-15 (Santa Barbara Amorphous-15). Their results showed that SBA-15 exhibited adsorption capacities superior to those of MCM-41, which is probably attributable to its two-dimensional biporous (micro-/mesoporous) system [14, 15]. Hung et al. [16] investigated the adsorption behaviors of acetone vapors over MCM-41 and ZSM-5 (Zeolite Socony Mobil–5). They demonstrated that MCM-41 revealed better adsorption capability and regeneration ability than the ZSM-5 zeolite, an adsorbent used in commercialized zeolite rotor concentrators [15, 16]. The adsorption of acetone and toluene on dealuminated Y-zeolite was studied by Lee et al. [17]. Their results showed that the adsorption amount of acetone was higher than that of toluene at low temperatures, but its adsorption affinity was weaker. Su et al. [4] conducted a comparative study on the adsorption of acetone over activated carbons (AC). Their results demonstrated that different functional groups under the same conditions provided different non-electrostatic contribution and electrostatic contributions to acetone adsorption capacity. The electrostatic contribution of oxygen-containing functional groups was better than that of nitrogen-containing functional groups, and functional groups containing oxygen and hydrogen were better than the functional groups containing only oxygen. Humidity resulted in the pronounced decrease in the non-electrostatic contribution to all functional groups. However, electrostatic contribution is less affected by humidity [4].

In recent years, hydrophobic zeolites have been safely used in catalytic oxidation processes at high temperatures due to their non-flammability, thermal stability, and moisture resistance. Hydrophobic zeolites have high adsorption affinity for acetone under humid conditions [18]. The affinity of hydrophobic and hydrophilic molecules and the ratio of Si/Al atoms affect the adsorption performance of zeolite, and the adhesive may also affect the adsorption performance of zeolite. When the Si/Al ratio in the zeolite is larger in a humid environment, the hydrophobicity and the adsorption capacity of the adsorbent will be enhanced. Bhatia et al. [19] prepared AgY (Si/Al=40) and AgZSM-5 (Si/Al=140) with different Si/Al ratios, and carried out experiments on the adsorption of butyl acetate under a relative humidity (RH) of 35%. Results showed that the adsorption capacity of AgZSM-5 was about 35% better than that of AgY material [3]. Huang et al. [13] prepared ZSM-5 (Si/Al=50–300) zeolite adsorbents with different Si/Al ratios to adsorb toluene at RH=50% condition. The adsorption capacity (75 mg g^{-1}) of ZSM-5–300 (Si/Al=300) is higher than that of ZSM-5–50 (Si/Al=50) (49 mg g^{-1}) by about 35% [13]. Therefore, it appears that increasing the Si/Al ratio of zeolite can improve its hydrophobicity, increase the adsorption capacity of pollutants, and enable it to be less affected by moisture.

Consequently, in this study, a new design hydrophobicity monometallic material and bimetallic metal material was prepared and applied for the adsorption acetone at lower temperature (298–328 K) and RH=50%. The effect of different operating parameters (including different materials, humidity, temperature, pollutant concentration, residence time, and regeneration) on the efficiency of acetone treatment is discussed in this study.

2 Materials and methods
2.1 Materials preparation
In this study, Fe–Mn mixed bimetallic oxide materials were prepared by immersing 5 g of granular zeolite carrier (including NaY, HY, USY and ZSM-5 zeolite) in 250 mL of an aqueous solution containing 10% Fe(NO$_3$)$_3$·9H$_2$O or 10% Mn(NO$_3$)$_2$, and soaking for 1 h, and then placing the mixture in a sonic shock tank on ultra-high and shaking it for 30 min. The liquid was then filtered through a screen to obtain the solid content. After that, the solid content was placed in an oven, dried at a temperature of 105 °C for 2 h, and then placed in a crucible and calcined at 550 °C for 6 h in a high-temperature furnace. The prepared material was then cooled to room temperature to obtain monometallic materials loaded with Fe or Mn (abbreviated as 10-Fe-NaY, 10-Fe-HY, 10-Fe-USY, 10-Mn-USY and 10-Fe-ZSM-5), and bimetallic material loaded with Fe and Mn (10-Fe$_x$Mn$_y$-USY, x/y is the ratio of Fe content to Mn content, which can be 1:4, 1:2, 1:1, 2:1 and 4:1).

2.2 Materials characterization
The morphology of the material was measured using a Scanning Electron Microscopy (SEM) via Energy Dispersive X-ray Spectroscopy (EDS) analysis. The specific

surface area, pore size distribution, and pore volume were determined by performing nitrogen adsorption–desorption measurements with an ASAP 2020 apparatus using Brunauer–Emmett–Teller (BET) calculation methods. The Fourier Transform Infrared (FTIR) of the material was recorded to study the functional groups at room temperature. A Thermo Gravimetric Analysis (TGA) instrument with a heating rate of 20 °C min^{-1} was used to study the thermal properties of the material. The change in the metal valence state in the material, the interaction between the metal oxide and its support, and the activation energy of the oxide reduction reaction were determined by the Hydrogen-Temperature Programmed Reduction (H$_2$-TPR) technique.

2.3 Adsorption performance assessment

An acetone adsorption measurement was performed for NaY zeolite, HY zeolite, USY zeolite, ZSM-5, and AC in a fixed bed reactor (length: 70 cm, inside diameter: 3 cm, outside diameter: 3.4 cm) at 800 ppm under humid conditions. The hydrophobic adsorbent with the best adsorption capacity was then selected, and different experimental parameters such as different acetone concentrations (400, 600, 800 and 1000 ppm), the effect of different residence time (0.18, 0.36, 0.54, 0.72 s), different operating temperatures (298, 308, 318, 328 K) and regeneration were examined for their effects on the adsorption capacity of acetone. The adsorption run was performed using high purity acetone (99.9%) gas and the feed flow was controlled by a mass flow controller connected to the fixed bed reactor in the experimental setup. The breakthrough curve of acetone was obtained by a gas chromatograph. In this study, the accuracy and reliability of the standardized or internationally recognized method were verified by analysis of certified standards. Analytical accuracy, determined from replicate analysis of laboratory standards and samples was 97%. Method detection limits under the conditions described are 0.1 ppm for acetone.

2.4 Isothermal adsorption model

2.4.1 Langmuir isotherm model

Langmuir adsorption model use to describe adsorption of solution species onto solid adsorbents. Based on the theory derive an equation, which depicted a relationship between the number of active sites of the surface undergoing adsorption and pressure. Langmuir model is followed in Eq. (1) [20, 21]:

$$Q = \left(\frac{ab \times C_e}{1 + aC_e} \right) \tag{1}$$

Taking the inverse of both sides gives Eq. (2) as follows:

$$\frac{1}{Q} = \frac{1}{b} + \frac{1}{ab \times C_e} \tag{2}$$

Again, C_e is the equilibrium acetone initial concentration in the solution and Q is the amount of acetone adsorbed by the additive. a and b are Langmuir constants related to adsorption capacity and adsorption energy, respectively. Plotting Q^{-1} versus C_e^{-1} and measuring the slope and intercept of the plot, a and b can be directly interpreted [20, 21].

2.4.2 Freundlich isotherm model

The Freundlich equation or Freundlich adsorption isotherm, an adsorption isotherm, is an empirical relation between the adsorbate concentrations on the surface of an adsorbent to the adsorbate concentration in the air with which it is in contact. The Freundlich model is followed in Eq. (3) [20, 21]:

$$Q = KC_e^{\frac{1}{n}} \tag{3}$$

Taking the natural logarithm of both sides gives Eq. (4) as follows:

$$\ln Q = \ln K + \left(\frac{1}{n(\ln C_e)} \right) \tag{4}$$

Plotting $\ln Q$ versus $\ln C_e$, the values of the Freundlich constants of K and n can be directly interpreted from the plot as the intercept and slope if the data of adsorption experiment matches the above empirical model [20, 21].

2.4.3 Temkin isotherm model

This isotherm contains a factor that explicitly taking into the account of adsorbent–adsorbate interactions. By ignoring the extremely low and large value of concentrations, the model assumes that heat of adsorption of all molecules in the layer would decrease linearly rather than logarithmic with coverage. As implied in the equation, its derivation is characterized by a uniform distribution of binding energies was carried out by plotting the quantity sorbed q_e against lnC_e and the constants were determined from the slope and intercept. The model is given by the following Eqs. (5) and (6) [22]:

$$q_T = q_e = \frac{RT}{b} \ln(A_T C_e) \tag{5}$$

$$q_e = \left(\frac{RT}{b} \right) \ln A_T + \left(\frac{RT}{b} \right) \ln C_e \tag{6}$$

where, q_T is adsorption capacity simulated by Temkin isotherm model (mg g^{-1}), q_e is adsorption capacity at reaction equilibrium (mg g^{-1}), R is universal gas

constant (8.314 J mol^{-1} K^{-1}), T is temperature at 298 K, b is Temkin isotherm constant, A_T is Temkin isotherm equilibrium binding constant (L g^{-1}) and C_e is adsorption concentration at reaction equilibrium (ppm).

2.5 Adsorption kinetic model

2.5.1 Pseudo-first-order

A first order reaction depends on the concentration of only one reactant (a unimolecular reaction). The pseudo-first-order equation is given as following Eq. (7):

$$\frac{dq_t}{dt} = k_1(q_e - q_t) \tag{7}$$

where, q_t is the amount adsorbed at time t (mg g^{-1}). In addition, k_1 is the pseudo-first-order rate coefficient (min^{-1}) and t is the contact time (min). The integration of Eq. (7) with the initial condition, $q_t = 0$ at $t = 0$, leads to the following Eq. (8) [21, 23]:

$$log(q_e - q_t) = \log q_e - \frac{k_1}{2.303}t \tag{8}$$

2.5.2 Pseudo-second-order

A second order reaction depends on the concentrations of one second order reactant, or two first order reactants. The pseudo-second-order model is represented as following Eq. (9):

$$\frac{dq_t}{dt} = k_2(q_e - q_t)^2 \tag{9}$$

where, k_2 is the pseudo-second-order rate coefficient (mg g^{-1} min^{-1}). Integrating Eq. (9) and $q_t = 0$ at $t = 0$, the following Eq. (10) is obtained [21, 23]:

$$\frac{t}{q_t} = \frac{1}{k_2 q_e^2} + \frac{1}{q_e}t \tag{10}$$

2.5.3 Intra-particle diffusion model

The intra-particle diffusion model was also tested with rate processes usually expressed in terms of square root of time. So q_t or fraction metal sorbed is plotted against $t^{1/2}$ as follow [24, 25]:

$$q_t = f\left(t^{1/2}\right) \tag{11}$$

The rate constant for intra-particle diffusion (k_i) at different initial concentrations is determined using the following Eq. (12):

$$q_t = k_i t^{1/2} \tag{12}$$

where, k_i is in mg g^{-1} media min$^{-1/2}$.

3 Results and discussion

3.1 Characterization

In this study, a contact angle meter was used to analyze the contact angle between the surface of the material and the water droplet to understand whether the material was hydrophilic or hydrophobic. The results are shown the contact angles of 10-Fe-NaY, 10-Fe-HY, 10-Fe-USY, 10-Fe-ZSM-5 and 10-Fe$_1$Mn$_1$-USY are 89°, 113°, 126°, 63° and 110 °, respectively, as shown in Fig. 1. Therefore, 10-Fe-HY, 10-Fe-USY and 10-Fe$_1$Mn$_1$-USY are hydrophobic materials (contact angle > 90°), while 10-Fe-NaY and 10-Fe-ZSM-5 are hydrophilic materials (contact angle ˂ 90°). The main reason is that 10-Fe-USY has the largest Si/Al ratio (10.7), as shown in Table S1 of Supplementary Materials, resulting in 10-Fe-USY having the largest contact angle (126°), while 10-Fe-ZSM-5 has the smallest Si/Al ratio (4.8), resulting in 10-Fe-ZSM-5 having the smallest contact angle (63°). A larger Si/Al ratio results in a larger contact angle and thus a stronger hydrophobicity, since Si–OH groups can make water molecules stay on the pore wall surface. However, free water weakly interacts with material pore surface, because water molecules form amorphous groups through limited intermolecular hydrogen bonding [26]. Li et al. [26] show that the contact angle of ZSM-5/siliceous zeolite composites is 17°, which is much smaller than that of the 10-Fe-USY.

To understand the thermal stability of different iron materials and its feasibility at high temperature, this study conducted a thermo gravimetric analysis of 10-Fe-USY, 10-Fe-HY, 10-Fe-NaY, 10-Fe-ZSM-5 and 10-Fe$_1$Mn$_1$-USY, and analyzed the weight loss change of the material after heating. The results of this analysis are shown in Fig. 2. These results show that the weight loss changes in two stages at temperatures of 50–200 °C and 350–500 °C, respectively. In the first stage, the initial weight loss of 10-Fe-USY, 10-Fe-HY, 10-Fe-NaY, 10-Fe-ZSM-5 and 10-Fe$_1$Mn$_1$-USY is the weight loss of decomposed adsorbed water. This weight loss is about 2.56, 8.30, 12.13, 17.54 and 1.23 wt%, respectively. The weight loss of the second stage changed by about 1.20, 4.44, 8.22, 6.78 and 0.7 wt%, respectively, mainly due to the removal of the adhesive and the aggregation of silanol groups to form siloxane bond condensation. The total weight loss at 500 °C is 3.76, 12.74, 20.35, 24.32 and 1.12 wt%, respectively. The weight loss of each stage is summarized in Table S2. Therefore, the 10-Fe-USY and 10-Fe$_1$Mn$_1$-USY in this study has the best thermal stability and the operating temperature will not affect the structure of the 10-Fe-USY and 10-Fe$_1$Mn$_1$-USY material. These results are similar to those of Tsai [27]. The main reason is that the content of Si in USY is quite high (Si/Al: 10-Fe-USY > 10-Fe$_1$Mn$_1$-USY > 10-Fe-HY > 10-Fe-NaY > 10-Fe-

Nguyen *et al. Sustainable Environment Research* (2023) 33:15

Page 5 of 15

10-Fe-USY θ_c: 126°

10-Fe-HY θ_c: 113°

10-Fe-NaY θ_c: 89°

10-Fe-ZSM-5 θ_c: 63°
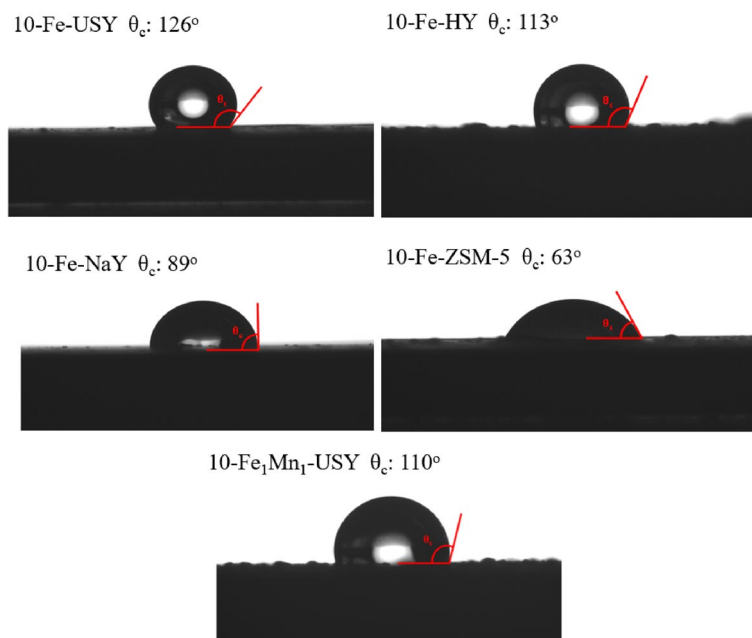
10-Fe$_1$Mn$_1$-USY θ_c: 110°

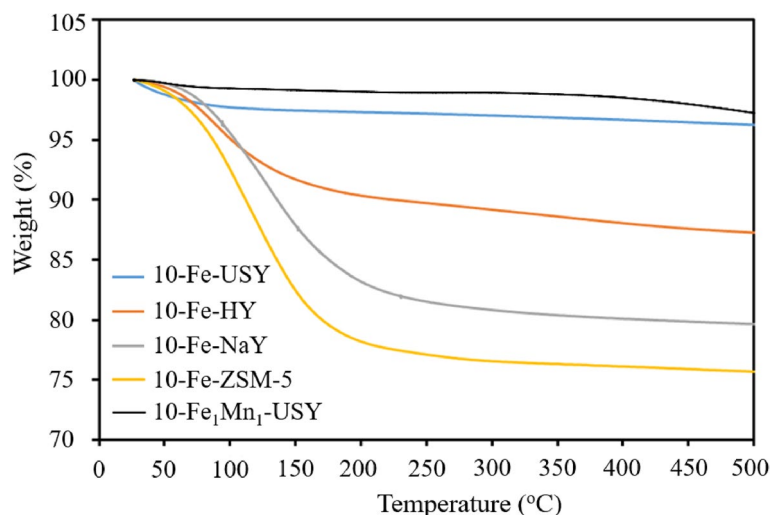**Fig. 1** Material contact angle analysis results

Fig. 2 Thermal stability analysis results for different iron materials

ZSM-5), therefore, it does not easily lose weight due to high temperature.

To understand the microstructure and morphology characterization of the USY zeolite, 10-Fe-USY, 10-Mn-USY, and 10-Fe$_1$Mn$_1$-USY materials, SEM was used to observe their appearance. The results show that the USY zeolite appears to comprise irregular quadrilateral particles with a smooth surface, as shown in Fig. 3a. The surface of the 10-Fe-USY, 10-Mn-USY, and

10-Fe$_1$Mn$_1$-USY is rough with fine particles, as shown in Fig. 3b-d. According to EDS analysis results, these particles are iron or manganese (Fig. S1). This demonstrates that the iron-manganese-containing composite materials have been successfully prepared in this study. The results of the analysis show that 10-Fe$_1$Mn$_1$-USY contains more iron and manganese than 10-Fe-USY and 10-Mn-USY, as shown in Table 1. The main reason is the synergistic relationship of Fe and Mn, which
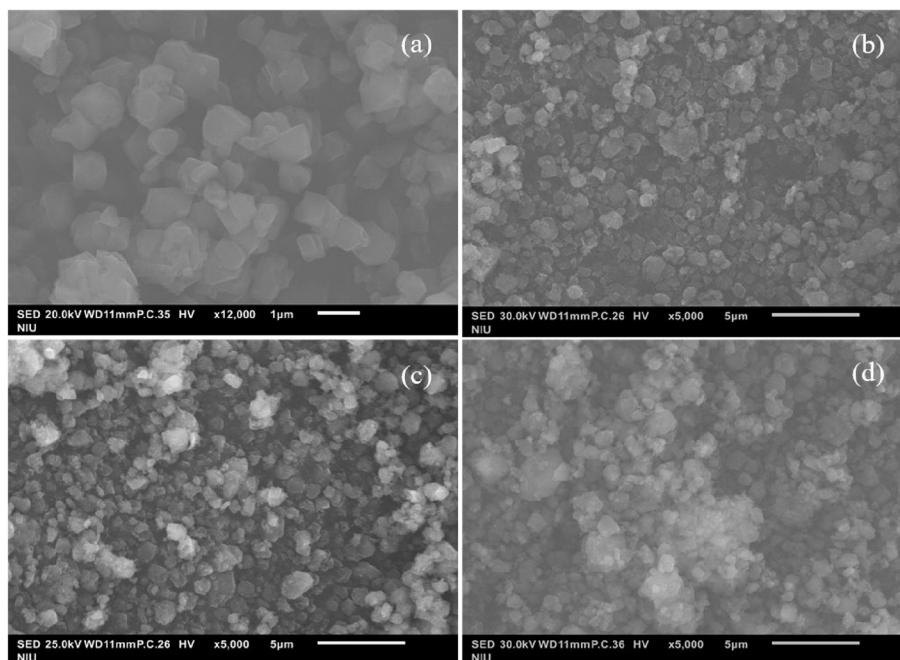
Fig. 3 SEM image of adsorption material: **a** USY Zeolite, **b** 10-Fe-USY, **c** 10-Mn-USY and **d** 10-Fe$_1$Mn$_1$-USY

Table 1 EDS analysis results of iron and manganese composites

Element	10-Fe-USY		10-Mn-USY		10-Fe$_1$Mn$_1$-USY	
	Weight %	Atomic %	Weight %	Atomic %	Weight %	Atomic %
Si (K)	26.14	17.23	20.90	13.50	15.73	10.18
O (K)	69.63	80.58	74.13	84.02	76.67	86.82
Al (K)	2.22	1.52	2.47	1.66	1.81	0.87
Fe (K)	2.01	0.67	–	–	2.97	1.10
Mn (K)	–	–	2.50	0.82	2.82	1.03
Totals	100		100		100	

makes it easier for Fe and Mn to form oxides on the surface of the material.

To understand the redox properties of ferromanganese material, this study conducted an H$_2$-TPR analysis and thermal conductivity detector (TCD), with the results shown in Fig. 4. The 10-Fe-USY material exhibits two reduction peaks. The first peak at 384 °C represents the reduction of Fe$_2$O$_3$ to Fe$_3$O$_4$, and the second peak at 496 °C represents the reduction of Fe$_3$O$_4$ to FeO. The 10-Mn-USY material also exhibits two reduction peaks, the first 354 °C corresponding to the reduction of MnO$_2$ to Mn$_2$O$_3$, and the second at 459 °C corresponding to the reduction of Mn$_2$O$_3$ to Mn$_3$O$_4$. There are four reduction peaks with the bimetallic 10-Fe$_1$Mn$_1$-USY material. The first peak at 303 °C is the reduction of MnO$_2$ to Mn$_2$O$_3$, the second at 320 °C is the reduction of Fe$_2$O$_3$ to Fe$_3$O$_4$, the third at 442 °C is the reduction of Mn$_2$O$_3$ to Mn$_3$O$_4$,

and the fourth at 484 °C corresponds to the reduction of Fe$_3$O$_4$ to FeO. These results are similar to those of Qin et al. [28] who also observed that 10Fe-15Mn-Al$_2$O$_3$ has four peaks at 310, 380, 530 and 580 °C, mainly due to the interaction between Fe and Mn elements, meaning that the iron-manganese-containing material improves the redox performance and reduces the reduction temperature. Therefore, the use of iron-manganese-containing material can treat acetone gas at low temperatures and improve the conversion efficiency.

To investigate the contribution, chemical state and electronic structure of the prepared iron-manganese-containing material, XPS measurements were performed on 10-Fe-USY, 10-Mn-USY and 10-Fe$_1$Mn$_1$-USY. Figure S2(a) shows the peaks of the 10-Fe-USY fitting results. The peak at 710.5 and 723.9 eV are the binding energies of Fe^{2+}, and the peak at 713.4 and 727.1 eV are the
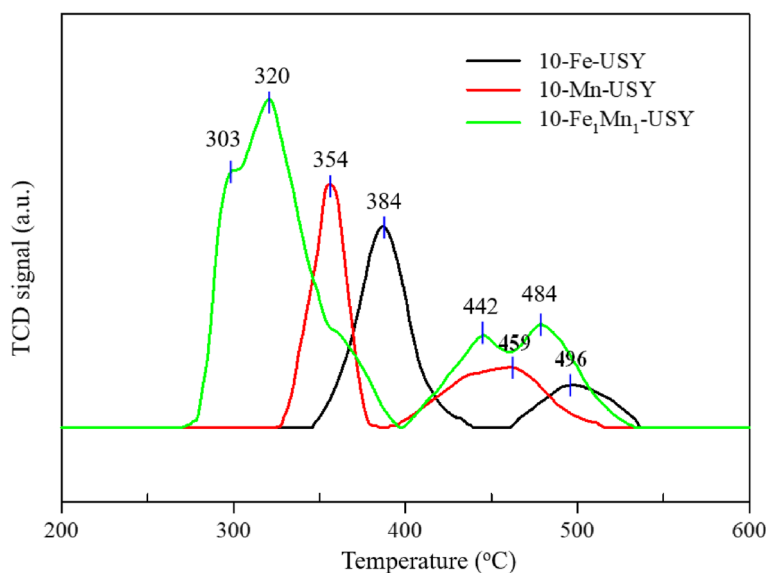
Fig. 4 H_2-TPR analysis results for different materials

binding energies of Fe^{3+}. Figure S2 (b) shows the peaks of the 10-Mn-USY fitting results. The peaks at 641.8 and 654.4 eV are the binding energies of Mn^{3+}, while the peak at 644.7 eV is the binding energy of Mn^{4+}. Figure S2 (c) shows the peaks of the 10-Fe$_1$Mn$_1$-USY fitting results. The peaks at 710.6 and 723.6 eV are the binding energies of Fe^{2+}, while the peaks at 713.4 and 726.9 eV represent the binding energies of Fe^{3+}. The peaks at 642.3 and 645.2 eV are the binding energies of Mn^{3+}, and 654.6 eV is the binding energy of Mn^{4+}, as shown in Fig. S2 (d).

We integrated the results of the peak area to calculate the proportion of the valence states of each element. The results, presented in Table S3, show that the Fe^{3+}/Fe^{2+} ratios of 10-Fe-USY and 10-Fe$_1$Mn$_1$-USY are 0.79 and 0.88, respectively. The Mn^{4+}/Mn^{3+} ratios of 10-Mn-USY and 10-Fe$_1$Mn$_1$-USY are 0.75 and 0.84, respectively. The O_{latt}/O_{ads} ratios of 10-Fe-USY, 10-Mn-USY and 10-Fe$_1$Mn$_1$-USY are 1.16, 1.23 and 1.51, respectively. The proportion of Fe^{3+}, Mn^{4+} and O_{latt} valence states that contribute to the acetone reaction with bimetallic catalyst 10-Fe$_1$Mn$_1$-USY is higher than that with single metal catalysts (10-Fe-USY, 10-Mn-USY). This is largely because the interaction between Fe and Mn is beneficial in increasing electron transfer and promoting vacancies, further increasing the ratio of Fe^{3+}, Mn^{4+} and O_{latt} containing bimetallic catalysts. That in turn improves the catalyst's ability to convert acetone. The results of this study are similar to those of Qin et al., who used iron and manganese metals modified onto γ-Al_2O_3 [28]. Through XPS analysis, it was found that the ratios of Fe^{3+}/Fe^{2+}, Mn^{4+}/Mn^{3+} and O_{latt}/O_{ads} were 0.89, 0.86 and 1.30, respectively, which was similar to the 10-Fe$_1$Mn$_1$-USY prepared in this

study [28]. The ratios of Fe^{3+}/Fe^{2+}, Mn^{4+}/Mn^{3+} and O_{latt}/O_{ads} are 0.88, 0.84 and 1.51, respectively.

In this study, nitrogen isothermal adsorption and desorption instrument was used to understand the surface area, pore size, and pore volume of different materials. The surface area of 10-Fe-USY, 10-Mn-USY, and 10-Fe$_1$Mn$_1$-USY was 709, 398, 422, and 444 m^2 g^{-1}, respectively. The pore volume of the materials was 0.41, 0.30, 0.32, and 0.46 cm^3 g^{-1}, respectively. The pore size of the materials was 2.41, 2.98, 2.85, and 2.95 nm, respectively. Results show that the modification of material by Mn/Fe metal will reduce its surface area and pore volume. This is because these metal ions fill in the pore walls and surfaces of the material, as shown in Table 2. The specific surface area of the 10-Fe$_1$Mn$_1$-USY materials prepared in this study is higher than that of 1Fe2MnC material (135 m^2 g^{-1}) prepared by Chen et al. [29].

3.2 Effect of different materials on acetone adsorption capacity

To understand the adsorption performance of different materials, the adsorption capacity of acetone was

Table 2 Specific surface area and pore size analysis results for different materials

Material	Surface area (m^2 g^{-1})	Pore volume (cm^3 g^{-1})	Pore size (nm)
USY zeolite	709	0.41	2.41
10-Fe-USY	398	0.30	2.98
10-Mn-USY	422	0.32	2.85
10-Fe$_1$Mn$_1$-USY	444	0.40	2.95

evaluated under the condition of containing water vapor (50%), and the adsorption materials of AC, ZSM-5, NaY zeolite, HY zeolite, and USY zeolite were compared at an adsorption temperature of 298 K, 0.18 s residence time, and 800 ppm inflow concentration. The breakthrough time is defined as the time when C/C_e is 0.1, and the saturation time is defined as the time when C/C_e is 0.9. The experimental results show that the breakthrough time of AC, ZSM-5, NaY zeolite, HY zeolite, and USY zeolite were 30, 35, 40, 45, and 50 min, respectively, and the saturation times were 75, 95, 110, 160, and 175 min, respectively. The capacities were 25.6, 44.3, 45.0, 59.0, and 65.3 mg g^{-1}, respectively, as shown in Fig. 5. Although AC has a high specific surface area (1551 m^2 g^{-1}), the affinity of AC with water is higher than that of acetone, which leads to the early adsorption of AC to reach saturation, lowering its adsorption capacity. However, USY zeolite has a higher Si/Al ratio (Si/Al = 10.7)

and a larger contact angle ($\theta_c = 130°$), resulting in good hydrophobicity of the material. Therefore, USY zeolite has a late adsorption penetration and reaches saturation later, giving it better adsorption capacity. Hsu [30] used Y-type zeolite and ZSM-5 molecular sieve to adsorb acetone, with adsorption capacities of 63.3 and 52.5 mg g^{-1}, respectively, showing that material containing ZSM-5 zeolite had poor adsorption capacity for acetone.

3.3 Effect of humidity conditions on acetone adsorption capacity

In this study, to understand whether the hydrophobic 10-Fe$_1$Mn$_1$-USY will affect its ability to adsorb pollutants in the state of water gas, the adsorption capacity of 10-Fe$_1$Mn$_1$-USY under dry and wet conditions was tested. The acetone adsorption tests were compared between dry (RH = 5%) and wet (RH = 50%) influent
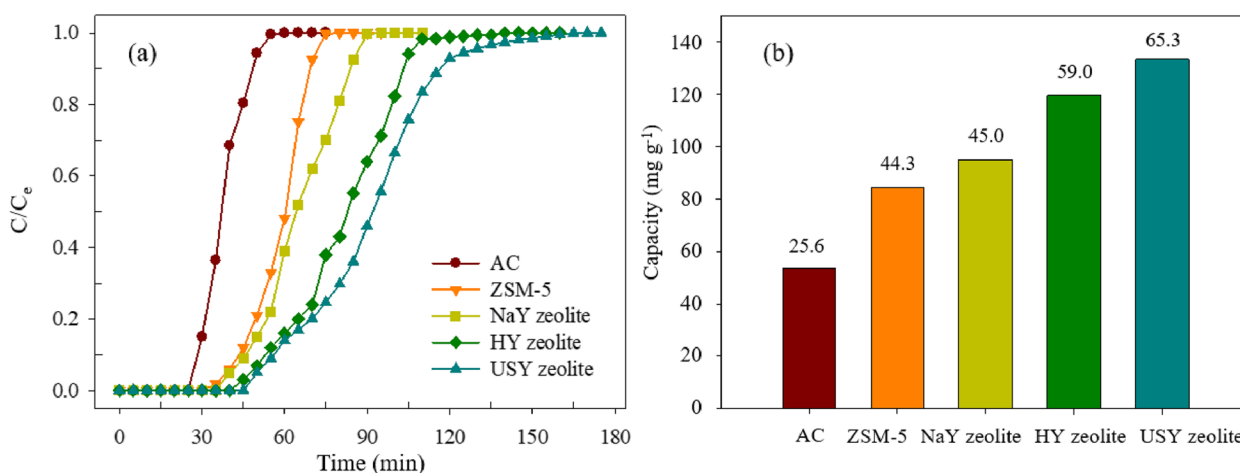

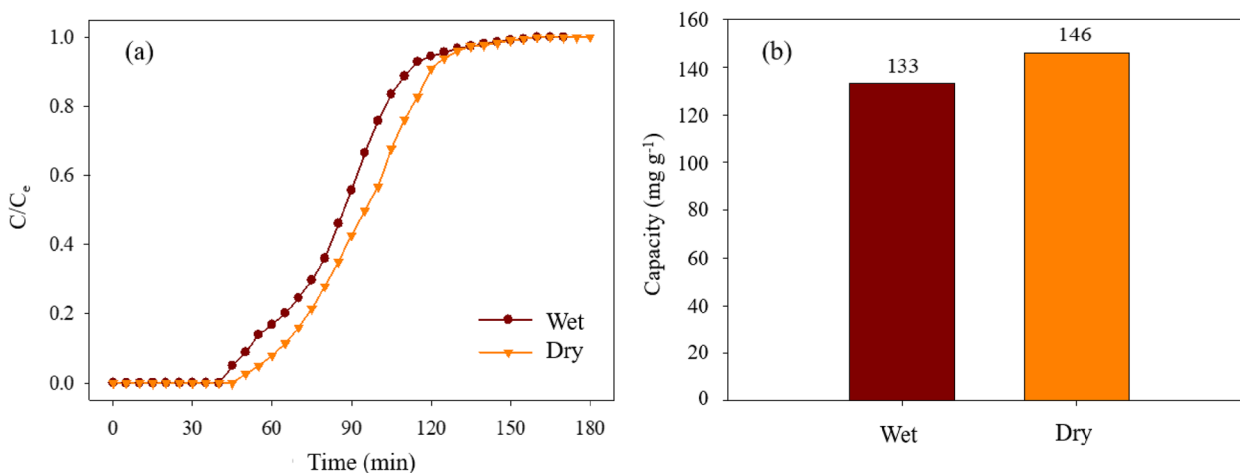**Fig. 5** Adsorption of acetone of different materials: **a** Removal efficiency, and **b** Adsorption capacity

Fig. 6 Effects on acetone adsorption under dry and wet conditions: **a** Removal efficiency, and **b** Adsorption capacity

Nguyen *et al. Sustainable Environment Research*   (2023) 33:15

Page 9 of 15

gases at an adsorption temperature of 298 K, a residence time of 0.18 s, and an influent acetone concentration of 800 ppm. Figure 6 shows that when the inflow gas is dry, the breakthrough time is 55 min, the saturation time is 180 min, and the adsorption capacity is 146 mg g^{-1}. When it is wet, the breakthrough time is 50 min, the saturation time is 175 min, and the adsorption capacity is 133 mg g^{-1}. The results showed that RH had no obvious influence on the acetone adsorption performance, which suggests that this material has good hydrophobic ability. Su et al. [4] has shown the humidity resulted in the pronounced decrease in the adsorption contribution to AC materials. However, adsorption contribution of 10-Fe$_1$Mn$_1$-USY material is less affected by humidity in this study.

3.4 Effect of different influent concentrations on acetone adsorption capacity

To understand the effect of different influent concentrations (400, 600, 800, and 1000 ppm) on the adsorption capacity of acetone in this study, 10-Fe$_1$Mn$_1$-USY material was used to conduct adsorption tests under the conditions of an adsorption temperature of 298 K and a residence time of 0.18 s. Figure 7 shows that as the inflow concentration increases, the adsorption penetration time and adsorption saturation time both decline. The penetration times were 120, 80, 55, and 35 min, respectively, while the saturation times were 220, 195, 180, and 155 min, respectively. The adsorption capacities were 116, 134, 146, and 157 mg g^{-1}, respectively, when the concentrations were 400, 600, 800, and 1000 ppm. These results show that when the acetone inflow concentration is higher, the adsorption capacity of the material improves, but the penetration time and saturation time

fall. The main reason is that with the increase of the acetone inflow concentration, the number of molecules that can be adsorbed by the material increases, raising the chance of contact between the material and acetone molecules, making it easy for the adsorption material to reach saturation earlier. The experimental results are similar to those of Hong et al. [31] and Ma and Ruan. [32]. As the inflow concentration of pollutants increases, the number of molecules that can be adsorbed by MCM-41 in the airflow also increases, resulting in a relative increase in the adsorption capacity of MCM -41, but the adsorption material will reach saturation earlier.

3.5 Effect of different residence time on acetone adsorption capacity

In this study, to understand the effect of different residence times (0.18, 0.36, 0.54, and 0.72 s) on the adsorption capacity of acetone, 10-Fe$_1$Mn$_1$-USY material was used to conduct adsorption tests under the conditions of an adsorption temperature of 298 K and an acetone inflow concentration of 800 ppm. Figure 8 shows that as the residence time increases, the adsorption penetration time and adsorption saturation time also increase. The penetration times were 55, 90, 115, and 130 min, respectively, while the saturation times were 180, 245, 310, and 365 min, respectively, and the adsorption capacities were 146, 139, 124, and 107 mg g^{-1}, respectively, when the residence times were 0.18, 0.36, 0.54, and 0.72 s, respectively. These results show that when the acetone residence time is shorter, the adsorption capacity of the material rises, but the penetration time and saturation time fall. The main reason is that the surface pressure of the material increases, which increases the driving force for the acetone to enter the pores, which is conducive to the capture
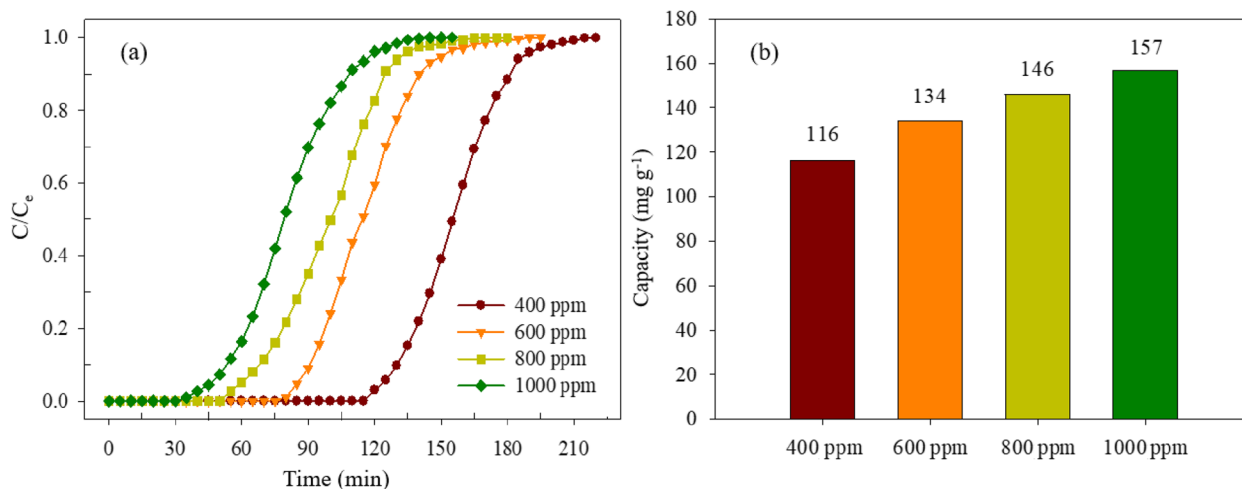

Fig. 7 Effects of different influent concentrations on acetone adsorption: **a** Removal efficiency, and **b** Adsorption capacity
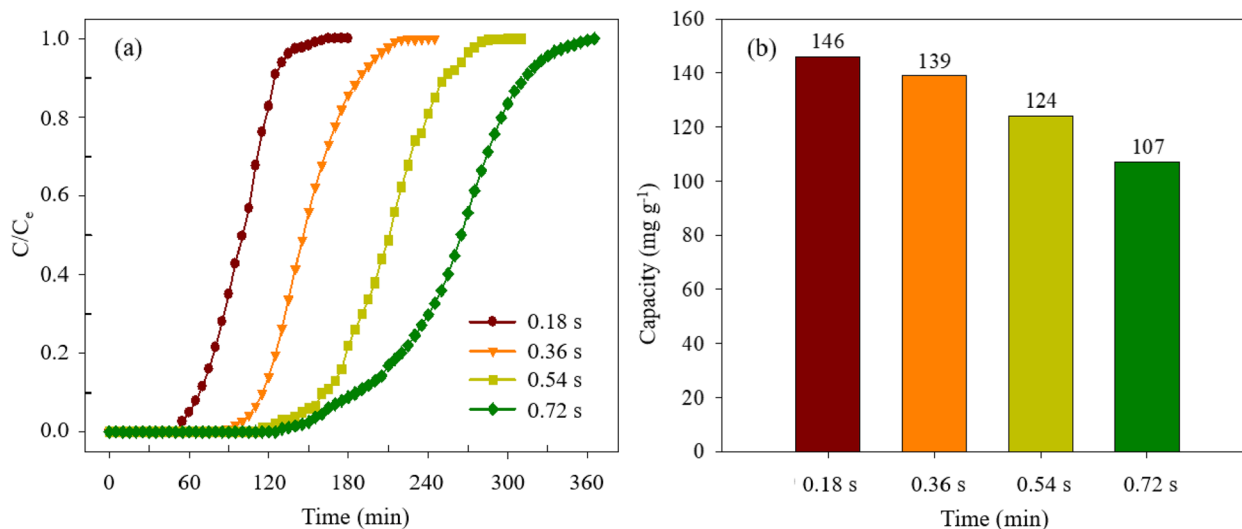
Fig. 8 Effect of different residence time on acetone adsorption: **a** Removal efficiency, and **b** Adsorption capacity

of acetone molecules, giving the 10-Fe$_1$Mn$_1$-USY material an increased adsorption capacity for acetone.

3.6 Effect of different temperatures on acetone adsorption capacity

This study examined the effect of different temperatures (298, 308, 318, and 328 K) on the adsorption capacity of 10-Fe$_1$Mn$_1$-USY material with an acetone inflow concentration of 800 ppm and a residence time of 0.18 s. The results are shown in Fig. 9. The adsorption capacity of 10-Fe$_1$Mn$_1$-USY material for acetone gradually fell as temperature rose. The penetration times were 45, 40, 35, and 30 min, respectively, and

the adsorption capacities were 146, 136, 119, and 109 mg g^{-1}, respectively. The penetration time is earlier and the adsorption capacity is reduced when the temperature increases. The main reason is that under high temperature adsorption, the acetone gas is prone to violent collisions, meaning that the surface adsorption sites of the 10-Fe$_1$Mn$_1$-USY material cannot effectively capture the acetone gas, resulting in the rapid passage of the acetone gas through the adsorption material. These results are similar to those of Tsai [27], who found that a lower reaction temperature is beneficial to the adsorption reaction.
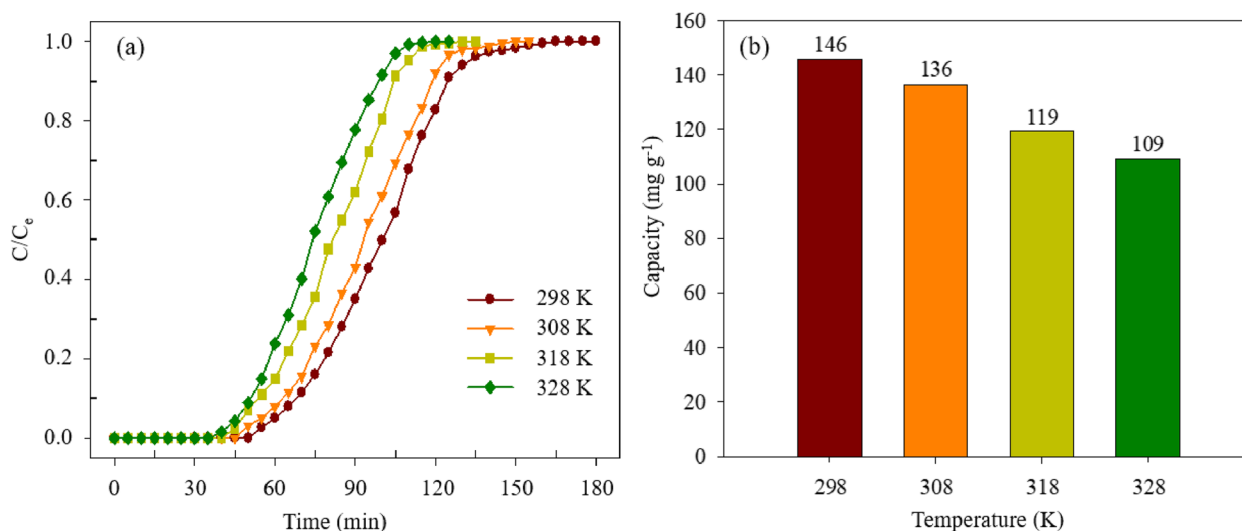

Fig. 9 Effect of different temperatures on acetone adsorption: **a** Removal efficiency, and **b** Adsorption capacity

3.7 Adsorbent material regeneration test

To determine whether the 10-Fe_1Mn_1-USY material can be reused, the adsorbed saturated material was desorbed and regenerated at high temperature (473 K, heating rate: 5 °C min^{-1}) under air condition. In this study, the adsorption capacity of 10-Fe_1Mn_1-USY before adsorption and after three cycles of desorption and regeneration were compared at an adsorption temperature of 298 K, a residence time of 0.18 s, and an influent concentration of 800 ppm. The results are shown in Fig. 10. The adsorption capacity of the fresh adsorbent was 146 mg g^{-1}, and the adsorption capacities of the materials after the first, second, and third desorption and regeneration were 123, 110, and 108 mg g^{-1}, respectively. The adsorption capacity of 10-Fe_1Mn_1-USY material decreased by about 27% after three cycles of desorption and regeneration. The adsorption behavior of 10-Fe_1Mn_1-USY material is a form of reversible physical adsorption behavior, making it a regenerable adsorbent. The reason for the decrease in adsorption capacity is that during the heating and desorption process, the 10-Fe_1Mn_1-USY material is lost due to the heating of the material surface, resulting in the loss of adsorption sites.

3.8 Isothermal adsorption model simulation results

Langmuir, Freundlich, and Temkin models have been proven to be the most reliable and widely used in adsorption systems. Therefore, Langmuir, Freundlich, and Temkin models were used to perform the adsorption capacity of ferromanganese material in this study. The experimental results are fitted to the models and the most appropriate model is determined to estimate the maximum amount of adsorption associated with ferromanganese material. In addition, the simulation results can be judged whether the adsorption reaction is physical adsorption or chemical adsorption. The saturated adsorption capacity of 10-Fe_1Mn_1-USY at an adsorption temperature of 298 K and a residence time of 0.18 s and inflow concentrations of 400, 600, 800, and 1000 ppm was substituted into the Langmuir, Freundlich, and Temkin models to obtain the isothermal adsorption model of 10-Fe_1Mn_1-USY for acetone. The linear regression results of the Langmuir model, the Freundlich model, and the Temkin model are shown in Fig. S3. The regression correlation coefficients are 0.999, 0.998, and 0.999 respectively. The parameters of the correlation isotherm adsorption formula are summarized in Table 3 and Fig. S4. The actual adsorption capacity of various acetone concentrations was compared with the predicted adsorption capacity of the Langmuir, Freundlich, and Temkin models, when using 10-Fe_1Mn_1-USY, as shown in Table S4. The results show that the regression correlation coefficient of the Temkin model is relatively high ($R^2 = 0.999$), and the calculated value of the Temkin model is very close
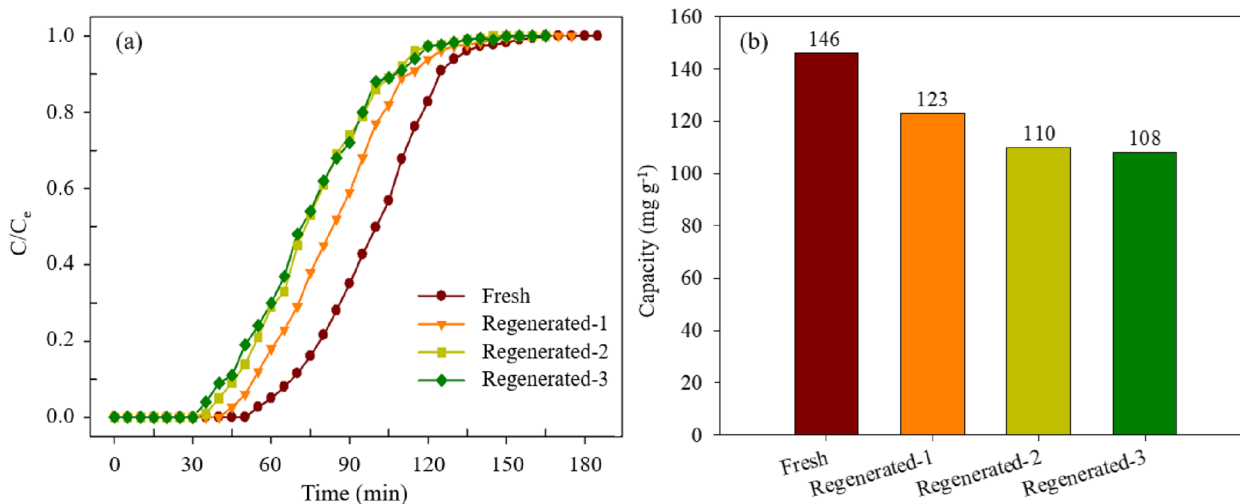

Fig. 10 Comparison of acetone adsorption capacity of materials after adsorption and desorption: **a** Removal efficiency, and **b** Adsorption capacity

Table 3 Parameters for isothermal adsorption analysis of acetone by Langmuir, Freundlich, and Temkin models

Langmuir			Freundlich			Temkin		
a (ppm^{-1})	b (mg g^{-1})	R^2	n	K (mg g^{-1})	R^2	A_T (g^{-1})	RT/b (J mol^{-1})	R^2
0.0034	201	0.997	3.4	19.5	0.998	0.035	44	0.999

to the actual value. It can be concluded that the adsorption of acetone using 10-Fe$_1$Mn$_1$-USY is more consistent with the Temkin model. The adsorption behavior of the 10-Fe$_1$Mn$_1$-USY for acetone is both monolayer and multi-layer adsorption simultaneously.

3.9 Adsorption kinetic model simulation results

The purpose of the kinetic adsorption model simulation is to understand the change of the adsorption capacity of acetone with the adsorption time, and to verify the possible adsorption mechanism by the model operation of the empirical formula. In this study, two adsorption kinetic models, the pseudo-first-order adsorption kinetic model and the pseudo-second-order adsorption kinetic model, were used to simulate and discuss the adsorption kinetics of the 10-Fe$_1$Mn$_1$-USY for acetone, and the most suitable adsorption kinetic model was obtained. The adsorption capacity per unit time of 10-Fe$_1$Mn$_1$-USY at an adsorption temperature of 298 K, a residence time of 0.18 s, and acetone concentrations of 400, 600, 800, and 1000 ppm was substituted into the adsorption kinetic model, and the appropriate kinetic

model evaluated. Table S5 shows the linear regression parameters of the adsorption kinetic model. The estimation results show that the correlation coefficient R^2 value of the pseudo-first-order kinetic model ranges from 0.886 to 0.907 and the reaction rate (k_1) is about 0.040 – 0.09 min^{-1}. The correlation coefficient R^2 value of the pseudo-second-order adsorption kinetic model is in the range of 0.523 – 0.862 and the reaction rate (k_2) is about $1.2 \times 10^{-7} - 1.7 \times 10^{-5}$ g mg^{-1} min^{-1}. The kinetic analysis results show that the k_1 value has limited differences under various concentrations, but the k_2 value has larger differences, which indicates that the acetone adsorption kinetic behavior is more suited to the pseudo-first-order adsorption kinetic model, as shown in Fig. 11 a and b

To understand the internal diffusion during the adsorption of acetone using 10-Fe$_1$Mn$_1$-USY material, an analysis of its adsorption behavior was performed using the intra-particle diffusion model. Adsorption capacities of 10-Fe$_1$Mn$_1$-USY material at acetone concentrations of at 400, 600, 800, and 1000 ppm, an adsorption temperature of 298 K, and a residence time of 0.18 s were analyzed. Taking the adsorption capacity (q_t) as the ordinate, and
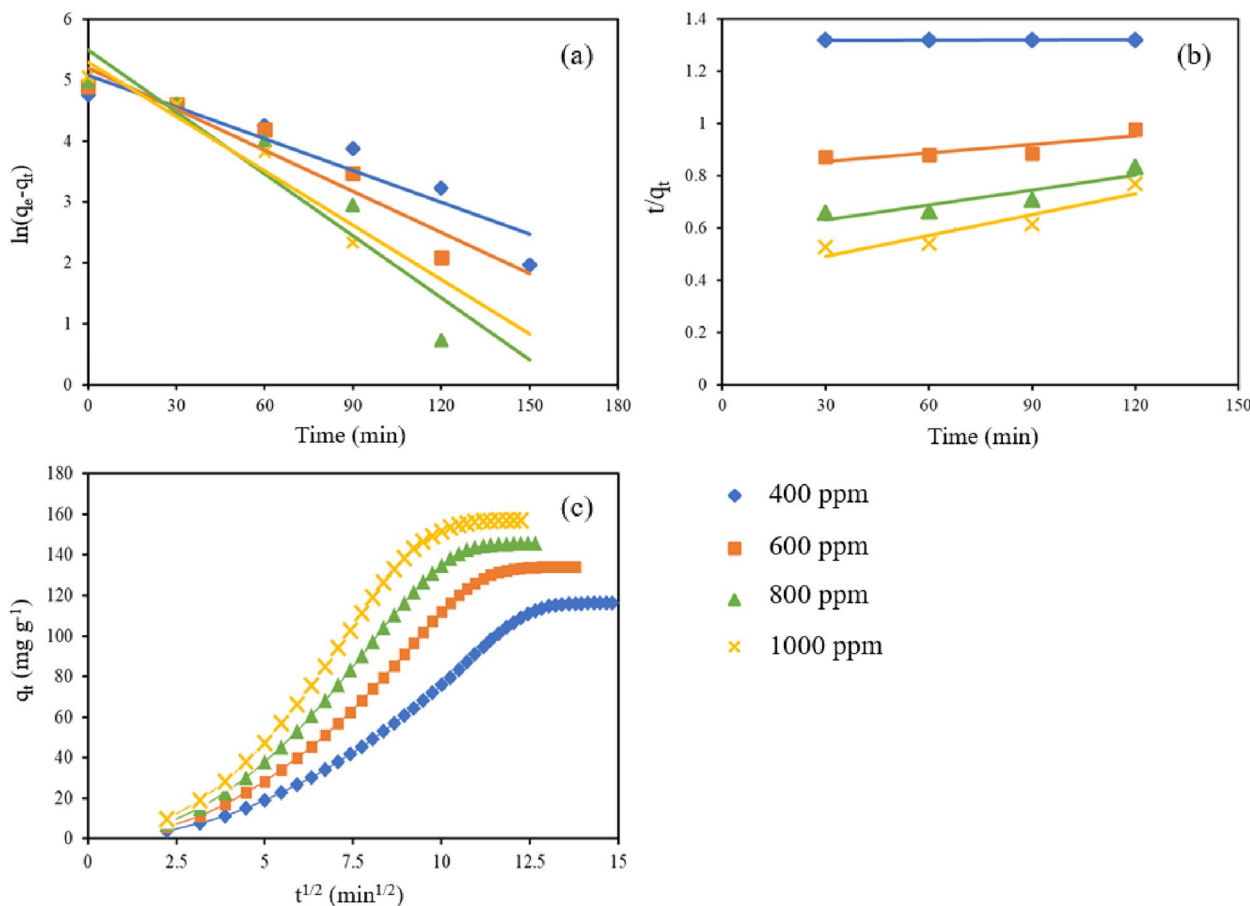

Fig. 11 Analysis results of (**a**) pseudo-first-order and (**b**) pseudo-second-order adsorption kinetic models and (**c**) internal diffusion models

Nguyen *et al. Sustainable Environment Research*   (2023) 33:15

Page 13 of 15

taking the root of the adsorption time (t) as the abscissa, and performing the regression analysis, q_t and $t^{0.5}$ were obtained, as shown in Fig. 11c and Table S6. Figure 11c shows that the adsorption behavior curve has a three-stage curve. The first curve is the film diffusion rate (K_{Fd}), the second curve is the intra-particle diffusion rate (K_{Id}), and the third curve is the equilibrium phase diffusion rate (K_{Ed}). The reaction rate constant of diffusion in the process of the 10-Fe$_1$Mn$_1$-USY material adsorbing acetone may then be calculated. In this study, the K_{Fd} and the K_{Id} increased with an increase in the acetone concentration. These results indicated that the diffusion of acetone controlled the adsorption rate. These results are similar to those of Shiue et al. [33] and Shiue et al. [34] who found that in the adsorption of toluene using granular AC, the intra-particle diffusion constant also increased as the toluene concentration increased from 10 to 70 ppm.

3.10 Thermodynamic model simulation results

To investigate the activation energy of 10-Fe$_1$Mn$_1$-USY for acetone adsorption reaction at different temperatures, the pseudo-first-order kinetic model was used to calculate the adsorption reaction rate constants of 10-Fe$_1$Mn$_1$-USY at 298, 308, 318, and 328 K (k_1; 0.00067, 0.00087, 0.0013, and 0.0016 s^{-1}, respectively). The natural logarithm value of the adsorption reaction rate constant (lnk_1) was used as the ordinate and the reciprocal temperature ($1/T$) as the abscissa. Figure S5 was obtained after the regression analysis. Results show that the activation energy (Ea) is 24.9 kJ mol^{-1} and the collision frequency factor (A) is 15.3 s^{-1}, as shown in Table 4.

In addition, the thermodynamic properties of 10-Fe$_1$Mn$_1$-USY for acetone adsorption at different temperatures were also investigated in this study. The changes in free energy (ΔG), enthalpy (ΔH) and entropy (ΔS) at the four temperatures of 298, 308, 318, and 328 K were investigated when the influent concentration was 800 ppm and the residence time was 0.18 s. The reciprocal temperature ($1/T$) was used as the abscissa and the natural logarithm value of the distribution coefficient (k_v) was used as the ordinate. Figure S6 was obtained after the regression analysis. Table 5 shows that the ΔG is negative,

Table 5 Thermodynamic model parameters of 10-Fe$_1$Mn$_1$-USY material

Temperature (K)	ΔG (kJ mol^{-1})	ΔH° (kJ mol^{-1})	ΔS° (J mol^{-1} K^{-1})
298	-9.7	-2.2	25.2
308	-10.0		
318	-10.3		
328	-10.5		

meaning that the adsorption reaction process is a feasible spontaneous adsorption reaction, and the ΔG value is between 0 and -20 kJ mol^{-1}, meaning that the adsorption is a form of physical adsorption. The ΔH value is negative (-2.2 kJ mol^{-1}), indicating that the adsorption process is an exothermic reaction. The ΔS value (25.2 J mol^{-1} K^{-1}) is greater than 0, which shows that the adsorption process is not self-sequential, and the entropy of the adiabatic system will not automatically decrease.

4 Conclusions

The 10-Fe$_1$Mn$_1$-USY material exhibits good adsorption capacity for acetone at a relative humidity of 50%. The main factors affecting the adsorption capacity are the contact angle, hydrophobicity, specific surface area, and Si/Al of the material. The adsorption capacity of 10-Fe$_1$Mn$_1$-USY rises with higher influent concentration and shorter residence time. Conversely, the adsorption capacity of 10-Fe$_1$Mn$_1$-USY material falls as the temperature increases. The isothermal adsorption and the kinetic adsorption behavior of the 10-Fe$_1$Mn$_1$-USY material for acetone is more suited to the Temkin isotherm adsorption model and the pseudo-first-order kinetic model. The adsorption of acetone by the 10-Fe$_1$Mn$_1$-USY material is dominated by intra-particle diffusion. Based on the thermodynamic analysis results, the adsorption behavior of the 10-Fe$_1$Mn$_1$-USY material for acetone is a form of physical adsorption, and a spontaneous and non-sequential reaction. TGA results show that 10-Fe$_1$Mn$_1$-USY materials have high stability under high temperature conditions, so future work projects can be extended to

Table 4 Arrhenius equation parameters of 10-Fe$_1$Mn$_1$-USY and comparison with other material

Material	Temperature (K)	k_1 (s^{-1})	E_a (kJ mol^{-1})	A (s^{-1})	R^2	Ref
10-Fe$_1$Mn$_1$-USY	298	0.00067	24.9	15.3	0.988	This study
	308	0.00087				
	318	0.00130				
	328	0.00162				
n-Ru/AC/*n*-ZnO	373–623	-	17.2	-	0.973	[35]
Cu-Al mixed oxide catalysts	423–498	-	44.3	-	-	[36]

Nguyen *et al. Sustainable Environment Research*   (2023) 33:15

Page 14 of 15

understand the conversion efficiency of $10\text{-}Fe_1Mn_1\text{-}USY$ materials to acetone.

Supplementary Information

The online version contains supplementary material available at https://doi.org/10.1186/s42834-023-00173-y.

Additional file1: Table S1. Resultsof adsorbent materials' XRF analysis. **Table S2.** Different iron materials' weight loss at various phases. **Table S3.** The ratio of thevalence state of each element in the catalyst. **Table S4.** Modeling parameters for isothermal adsorption models analysis. **Table S5.** Modeling parameters for pseudo-first-order and pseudo-second-order adsorption. **Table S6.** The findings of the 10-Fe1Mn1-USY material diffusion rate regression analysis. **Fig. S1.** EDS results of (a) 10-Fe-USY, (b) 10-Mn-USY and (c) 10-Fe1Mn1-USY materials. **Fig. S2.** XPS diagram of catalyst material: (a) 10-Fe-USY, (b) 10-Mn-USY and (c-d) $10\text{-}Fe_1Mn_1\text{-}USY$. **Fig. S3.** Results from the (a) Langmuir, (b) Freundlich, and (c) Temkin models using linear regression. **Fig. S4.** Results of isotherm adsorption model analysis. **Fig. S5.** Results of the Arrhenius equation study for the material $10\text{-}Fe_1Mn_1\text{-}USY$. **Fig. S6.** Results of the thermodynamic adsorption analysis for the material $10Fe_1Mn_1USY$.

Authors' contributions
Nhat-Thien Nguyen and Thi-Minh-Phuong Nguyen provided real test data, Alvin-R Caparanga and Yi-Ren Chiu supported the test data, Cong-Chinh Duong and Thi-Thanh Duong wrote the paper, Chung-Yu Guanand Gui-Bing Hong analyzed the test data, and Chang-Tang Chang organized the researched full structure. All authors read and approved the final manuscript.

Availability of data and materials
All data generated or analyzed during this study are examined by our group and certified for several times.

Declarations

Competing interests
The authors declare they have competing interests.

References
1. Yang HH, Gupta SK, Dhital NB. Emission factor, relative ozone formation potential and relative carcinogenic risk assessment of VOCs emitted from manufacturing industries. Sustain Environ Res. 2020;30:28.
2. Janfaza S, Kim E, O'Brien A, Najjaran H, Nikkhah M, Alizadeh T, et al. A nanostructured microfluidic artificial olfaction for organic vapors recognition. Sci Rep-Uk. 2019;9:19051.
3. Mirzaei A, Leonardi SG, Neri G. Detection of hazardous volatile organic compounds (VOCs) by metal oxide nanostructures-based gas sensors: a review. Ceram Int. 2016;42:15119–41.
4. Su ZB, Zhang YY, Huang LL, Wang SS, Zhu YD, Li LC, et al. Acetone adsorption on activated carbons: Roles of functional groups and humidity. Fluid Phase Equilibr. 2020;521:112645.
5. El Hammami Y, Zine-Dine K, Mir R, Midiouni T, Ait Hssain M. Numerical Simulation of Volatile Organic Compounds during Condensation in a Vertical Tube. Proceedings. 2019;38:21.
6. Li YJ, Chang HY, Yan H, Tian SL, Jessop PG. Reversible absorption of volatile organic compounds by switchable-hydrophilicity solvents: a case study of toluene with N,N-Dimethylcyclohexylamine. ACS Omega. 2021;6:253–64.
7. Jia Z, Barakat C, Dong B, Rousseau A. VOCs destruction by plasma catalyst coupling using AL-KO PURE air purifier on industrial scale. J Mater Sci Chem Eng. 2015;3:19–26.
8. van der Vaart DR, Vatvuk WM, Wehe AH. Thermal and catalytic incinerators for the control of VOCs. J Air Waste Manage. 1991;41:92–8.
9. More RK, Lavande NR, More PM. Mn supported on Ce substituted hydroxyapatite for VOC oxidation: Catalytic activity and calcination effect. Catal Lett. 2020;150:419–28.
10. Liu RY, Trinh MM, Chang MB. Photocatalytic removal of toluene with $CdIn_2S_4$/CNFs catalyst: effect of ozone addition. Sustain Environ Res. 2022;32:10.
11. Winayu BNR, Mao WH, Chu H. Combination of rGO/S, N/TiO_2 for the enhancement of visible light-driven toluene photocatalytic degradation. Sustain Environ Res. 2022;32:34.
12. Yu HC, You SW, Wang C, Deng JG, Hsi HC. Regeneration of beaded activated carbon saturated with volatile organic compounds by a novel electrothermal swing adsorption system. Sustain Environ Res. 2022;32:51.
13. Huang HF, Rong WJ, Gu YY, Chang RQ, Lu HF. Adsorption and desorption of VOCs on the ZSM-5 zeolite. Acta Scientiae Circumstantiae. 2014;34:3144–51 [in Chinese]. https://www.actasc.cn/hjkxxb/ch/reader/view_abstract.aspx?file_no=20140219001&flag=1 (Accessed 21 Feb 2023).
14. Zhang WW, Qu ZP, Li XY, Wang Y, Ma D, Wu JJ. Comparison of dynamic adsorption/desorption characteristics of toluene on different porous materials. J Environ Sci-China. 2012;24:520–28.
15. Zeng WT, Bai HL. Adsorption/desorption behaviors of acetone over micro-/mesoporous SBA-16 silicas prepared from rice husk agricultural waste. Aerosol Air Qual Res. 2016;16:2267–77.
16. Hung CT, Bai HL, Karthik M. Ordered mesoporous silica particles and Si-MCM-41 for the adsorption of acetone: a comparative study. Sep Purif Technol. 2009;64:265–72.
17. Lee DG, Kim JH, Lee CH. Adsorption and thermal regeneration of acetone and toluene vapors in dealuminated Y-zeolite bed. Sep Purif Technol. 2011;77:312–24.
18. Zaitan H, Manero MH, Valdes H. Application of high silica zeolite ZSM-5 in a hybrid treatment process based on sequential adsorption and ozonation for VOCs elimination. J Environ Sci-China. 2016;41:59–68.
19. Bhatia S, Abdullah AZ, Wong CT. Adsorption of butyl acetate in air over silver-loaded Y and ZSM-5 zeolites: Experimental and modelling studies. J Hazard Mater 2009;163:73–81.
20. Uddin MT, Islam MS, Abedin MZ. Adsorption of phenol from aqueous solution by water hyacinth ash. ARPN J Eng Appl Sci. 2007;2:2.
21. Nguyen NT, Chen SS, Nguyen NC, Nguyen HT, Tsai HH, Chang CT. Adsorption of methyl blue on mesoporous materials using rice husk ash as silica source. J Nanosci Nanotechno. 2016;16:4108–14.
22. Venkatesha TG, Nayaka YA, Chethana BK. Adsorption of Ponceau S from aqueous solution by MgO nanoparticles. Appl Surf Sci. 2013;276:620–7.
23. Simonin JP. On the comparison of pseudo-first order and pseudo-second order rate laws in the modeling of adsorption kinetics. Chem Eng J. 2016;300:254–63.
24. Guibal E, Milot C, Tobin JM. Metal-anion sorption by chitosan beads: Equilibrium and kinetic studies. Ind Eng Chem Res. 1998;37:1454–63.
25. Weber WJ, Morris JC. Kinetics of adsorption on carbon from solution. J Sanit Eng Div. 1963;89:31–59.
26. Li RN, Chong SJ, Altaf N, Gao YS, Louis B, Wang Q. Synthesis of ZSM-5/siliceous zeolite composites for improvement of hydrophobic adsorption of volatile organic compounds. Front Chem. 2019;7:505.
27. Tsai HH. Acetone and hexamethyldisilazane removal with mesoporous materials and catalysts prepared from calcium fluoride sludge [Master's thesis]. Yilan City: National Ilan Univ; 2015 [in Chinese]. https://hdl.handle.net/11296/uhj8jk (Accessed 07 Mar 2023).
28. Qin LB, Huang XM, Zhao B, Wang Y, Han J. Iron oxide as a promoter for toluene catalytic oxidation over $Fe\text{–}Mn/\gamma\text{-}Al_2O_3$ catalysts. Catal Lett. 2020;150:802–14.

29. Chen CK, Chen JJ, Nguyen NT, Le TT, Nguyen NC, Chang CT. Specifically designed magnetic biochar from waste wood for arsenic removal. Sustain Environ Res. 2021;31:29.

30. Hsu CS. Adsorption/desorption studies of volatile organic compounds generated from the optoelectronics industry by zeolites [Master's thesis]. Kaohsiung: National Sun Yat-Sen Univ; 2006 [in Chinese]. https://hdl.handle.net/11296/7uw77e (Accessed 22 Feb 2023).

31. Hong GB, Ruan RT, Chang CT. MCM-41 from spent glasses for volatile organic compounds treatment. Chem Eng J. 2013;215–6:472–8.

32. Ma CM, Ruan RT. Adsorption of toluene on mesoporous materials from waste solar panel as silica source. Appl Clay Sci. 2013;80–1:196–201.

33. Shiue A, Kang YH, Hu SC, Jou GT, Lin CH, Hu MC, et al. Vapor adsorption characteristics of toluene in an activated carbon adsorbent-loaded nonwoven fabric media for chemical filters applied to cleanrooms. Build Environ. 2010;45:2123–31.

34. Shiue A, Den W, Kang YH, Hu SC, Jou GT, Lin CH, et al. Validation and application of adsorption breakthrough models for the chemical filters used in the make-up air unit (MAU) of a cleanroom. Build Environ. 2011;46:468–77.

35. Al-Rabiah AA, Boz I, Akhmedov VM, Mostafa MMM, Bagabas AA. Highly selective gas-phase catalytic hydrogenation of acetone to isopropyl alcohol. Catalysts. 2022;12:1251.

36. Basu S, Pradhan NC. Kinetics of acetone hydrogenation for synthesis of isopropyl alcohol over Cu-Al mixed oxide catalysts. Catal Today. 2020;348:118–26.

Publisher's Note